iScience

CellPress
OPEN ACCESS

Article

3D Printable concentrated liquid metal composite with high thermal conductivity

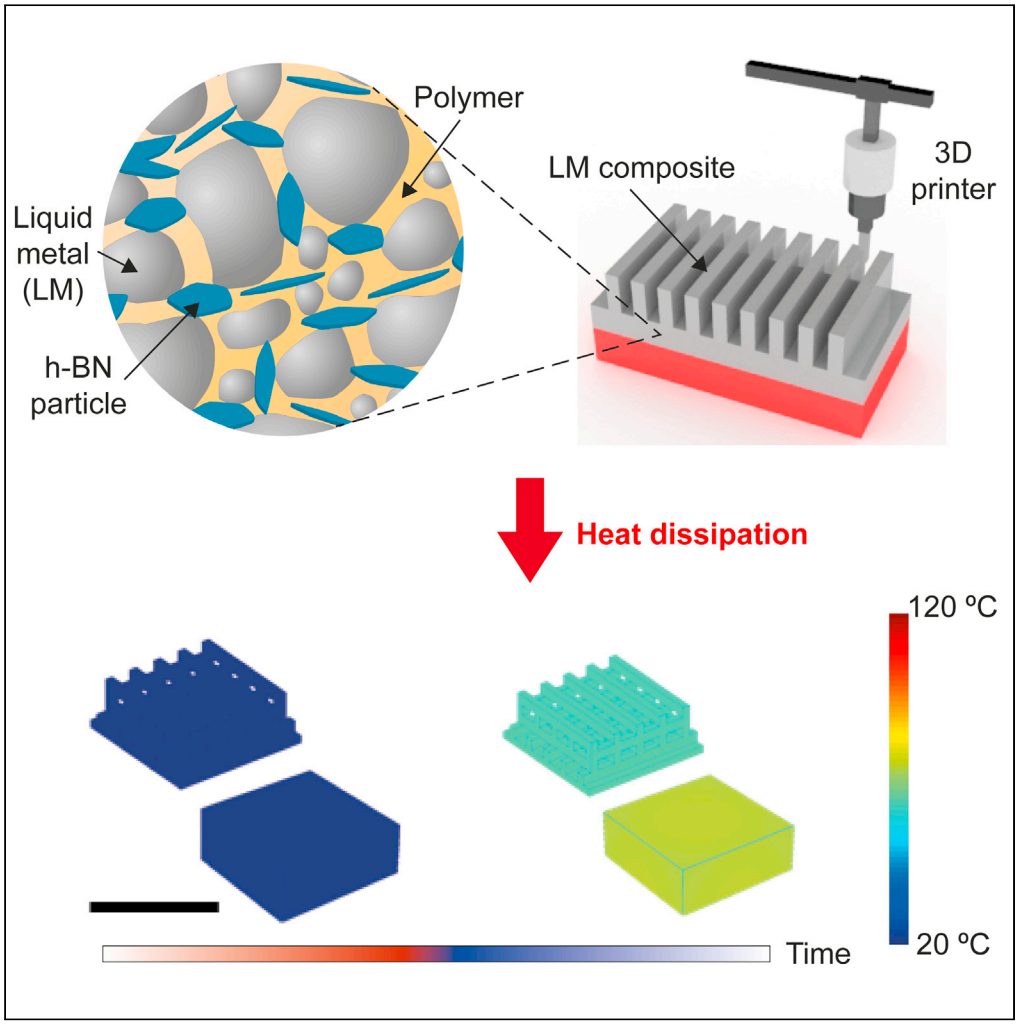

Sumin Moon, Hanul Kim, Kyoungmun Lee, Jinwon Park, Yunho Kim, Siyoung Q. Choi

sqchoi@kaist.ac.kr

Highlights

Liquid metal (LM) composites overcome thermal conductivity (*k*)-processability trade-off

High filler fraction and h-BN introduced between LM droplets result in high *k*

Concentrated LM composites are processable at room temperature and 3D printable

This combination of high *k* and processability enables rapid heat dissipation

Moon et al., iScience *24*, 103183
October 22, 2021 © 2021 The Authors.
https://doi.org/10.1016/j.isci.2021.103183

iScience

CellPress
OPEN ACCESS

Article

3D Printable concentrated liquid metal composite with high thermal conductivity

Sumin Moon,[1] Hanul Kim,[1] Kyoungmun Lee,[1] Jinwon Park,[1] Yunho Kim,[2] and Siyoung Q. Choi[1,3,*]

SUMMARY

Heat dissipation materials in which fillers are dispersed in a polymer matrix typically do not exhibit both high thermal conductivity (*k*) and processability due to a trade-off. In this paper, we fabricate heat dissipation composites which overcome the trade-off using liquid metal (LM). By exceeding the conventional filler limit, ten times higher *k* is achieved for a 90 vol% LM composite compared with *k* of 50 vol % LM composite. Further, an even higher *k* is achieved by introducing h-BN between the LM droplets, and the highest *k* in this study was 17.1 W m^{-1} K^{-1}. The LM composite is processable at room temperature and used as inks for 3D printing. This combination of high *k* and processability not only allows heat dissipation materials to be processed on demand under ambient conditions but it also increases the surface area of the LM composite, which enables rapid heat dissipation.

INTRODUCTION

The importance of heat dissipation has been emphasized for many applications, such as electronic devices, LEDs, power modules, and automobiles because heat accumulation shortens the lifetime of the devices, lowers efficiency, and causes malfunction of equipment due to thermal stress and thermal expansion (Chung et al., 2009; Yang et al., 2021). Generally, heat generation per unit volume in electronic devices rapidly increases as the devices become miniaturized and highly integrated (Cinchetti et al., 2017; Zhou et al., 2007). One way to effectively dissipate heat from small heat sources with limited surface area is thermal conduction, so typically high thermal conductivity materials are required. At the same time, these materials need to be processed to obtain the desired structure for practical applications and to increase the surface area for rapid heat dissipation. Accordingly, various high thermal conductivity materials (e.g., Cu, AlN, and BN) have been proposed (Boudenne et al., 2005; Chang et al., 2006; Xu et al., 2001), but these materials such as metals or sometimes ceramics are typically difficult to process due to their high melting temperature. An appropriate alternative would be polymeric materials that can be easily processed, but their relatively low thermal conductivity compared with metals and ceramics makes them difficult to use.

To overcome this limitation, a conventional way to achieve both high thermal conductivity (*k*) and processability is a polymeric composite with high *k* fillers (e.g., metal (Boudenne et al., 2005; Kumlutaş et al., 2003), carbon-based (Biercuk et al., 2002; Liu et al., 2004; Teng et al., 2011), and ceramic powders (Hu et al., 2016; Ishida and Rimdusit, 1998; Ohashi et al., 2005; Xu et al., 2001; Xu and Chung, 2000; Yung and Liem, 2013)), which takes advantage of both the fillers and the matrix. However, in practical applications, it is difficult to achieve both high thermal conductivity and processability due to trade-off relation; to achieve high thermal conductivity, a high volume fraction of solid fillers must be contained in the composite, which results in poor processability. Otherwise, low volume fractions of fillers do not provide high thermal conductivity.

To achieve both high thermal conductivity and processability, an alternative is to use a liquid filler with a high *k*. Compared with solid fillers, it is relatively easier to include a high fraction of liquid fillers in a matrix, and even higher fraction than 70 vol% is possible. The large volume fraction of fillers guarantees a high thermal conductivity, and the liquid fillers can be advantageous for processing because both the filler and polymer matrix are deformable. Liquid metal (LM), such as eutectic gallium indium (EGaIn, 75.5% Ga, 24.5% In, by weight) could be a replacement for the solid filler, as it has relatively high *k* (26.4 W m^{-1} K^{-1}), metallic conductivity, low melting temperature (melting point = 288.6 K), and low toxicity (Dickey, 2014; Yu and Kaviany, 2014).

LM has been applied in various studies by utilizing its electrical conductivity (Mineart et al., 2013; Park et al., 2019a, 2019b; Wissman et al., 2017) or thermal conductivity, and in particular, the thermal conductivity of

[1]Department of Chemical and Biomolecular Engineering and KINC, Korea Advanced Institute of Science and Technology (KAIST), Daejeon 34141, Korea

[2]Advanced Functional Polymers Research Center, Korea Research Institute of Chemical Technology (KRICT), Daejeon 34114, Korea

[3]Lead contact

*Correspondence: sqchoi@kaist.ac.kr

https://doi.org/10.1016/j.isci.2021.103183

This is an open access article under the CC BY-NC-ND license (http://creativecommons.org/licenses/by-nc-nd/4.0/).

LM attracted attention in cooling applications (Deng and Liu, 2010; Ma and Liu, 2007; Yang and Liu, 2018; Zhu et al., 2016). In addition, the unique features of LM allow it to be used as fillers in composites. The purpose of fabricating LM composite was also focused on using its electrical conductivity (Blaiszik et al., 2012; Fassler and Majidi, 2015; Markvicka et al., 2018; Saborio et al., 2020; Tang et al., 2019; Xin et al., 2019) or high thermal conductivity (Bartlett et al., 2017; Jeong et al., 2015; Mei et al., 2014). Mei et al., previously reported 5.27 W m^{-1} K^{-1} for LM filled thermal grease by dispersing LM droplets inside methyl silicone oil (Mei et al., 2014). For LM filled polymer composite, thermal conductivity of 2.2 W m^{-1} K^{-1} was reported for 66 vol% of LM dispersed in a silicone elastomer (Jeong et al., 2015), and Bartlett et al. reported thermal conductivity of 9.8 W m^{-1} K^{-1} in the stretched direction by dispersing 50% of LM in a soft elastomer (Bartlett et al., 2017).

Processing the LM composite in the previous research was mainly limited to molding as LM flowed as "liquid". This flow behavior as liquid makes LM a promising material candidate for various applications (Bartlett et al., 2017; Dickey, 2014; Jeong et al., 2015; Palleau et al., 2013; Zhu et al., 2013) but limits its applications at the same time. This crucial limit of processability has created the need for various approaches for processing LM such as filling/removing LM into/from a tube (Khan et al., 2014a, 2014b; Lin et al., 2017), direct writing/3D printing of LM (Ladd et al., 2013; Neumann and Dickey, 2020), direct writing of LM composite (Neumann et al., 2020; Rahim et al., 2021), and 3D printing of carbon nanotube/LM composites (Park et al., 2019a, 2019b). Among these efforts, Ladd et al., reported the oxide layer of the LM allows the LM itself to be used as a 3D printable material (Ladd et al., 2013). However, the target application is different from the electrically insulating LM polymer composite in this paper, since LM itself is electrically conductive liquid. In addition, the structure made of LM itself can collapse easily due to relatively low yield stress of LM. To be applied, additional packaging or LM with high melting point is sometimes required (Ladd et al., 2013; Wang and Liu, 2014). On the other hand, high yield stress of the LM polymer composite can prevent the structure from collapsing easily even without curing.

In this paper, we demonstrate a 3D printable concentrated LM composite with high thermal conductivity (Figure 1A). By increasing the volume fraction of LM (Φ_{LM}) above 0.7 and inserting high *k* particles between LM droplets, the maximum thermal conductivity through this approach is measured as high as 17.1 W m^{-1} K^{-1} and is isotropic in all directions, which is about 70% higher than that of the previous LM composites. Even at this high Φ_{LM}, the LM composite is electrically insulating, because electrically insulating polymer matrix and Ga_2O_3 clearly separate the LM droplets, disconnecting the electrical path in the LM composite. Moreover, unlike the previous LM composites, which were mainly processed by molding, our viscoelastic LM composite at high Φ_{LM} exhibited shear thinning behavior and suitable yield stress for 3D printing.

RESULTS AND DISCUSSION

As fabricated with solid filler, the LM composite in which EGaIn droplets are dispersed in an uncured NOA 68 polymer is made by a mechanical mixing process using a vortex mixer and a homogenizer, as shown in Figure 1B. When using polymers which can be applied as liquid such as epoxy resin, k_c and rheological properties of LM composites show similar tendencies (Figures S2 and S3). As the LM droplets are generated by shear mixing, more surface is exposed to O_2, and Ga_2O_3 is passivated on the LM droplets (Lin et al., 2015). Using this oxidation, oxide film is formed on the LM droplets, which acts as a stabilizer to prevent LM droplet coalescence. Figures 1C and 1F give a schematic illustration of the LM composite and a microscopic image of the corresponding LM composite (Φ_{LM} = 0.5). As shown in Figure 1F, the silvery droplet is LM and the black background is the polymer matrix. While non-spherical droplets were also created due to the oxide layer on its surface, most of the LM droplets were spherical due to the high interfacial tension of the LM (Khan et al., 2014a, 2014b). Figures 1D and 1G show a schematic illustration of the concentrated LM composite with $\Phi_{LM} \geq 0.7$ and its scanning electron microscope (SEM) image. As the droplets are clearly separated by thermal resistant polymers, LM droplets are stabilized without coalescence even at high LM fractions. Using a narrow distance between LM droplets at a high LM fraction, we add high *k* hexagonal boron nitride (h-BN) between LM droplets for more enhanced thermal conductivity, as shown in Figures 1E and 1H.

X-ray photoelectron spectroscopy (XPS) was performed on pure LM, LM composite, and LM composite with h-BN particles to investigate the surface chemical state (e.g., Ga 2p, In 3d, and B 1s) of the LM composite (Figure S4). Gallium mostly exists as gallium oxide (i.e., Ga^{3+}) and indium exists in a metallic state on the surface of pure LM. After dispersing the LM in the polymer, it was confirmed that the oxidation state of

CellPress
OPEN ACCESS

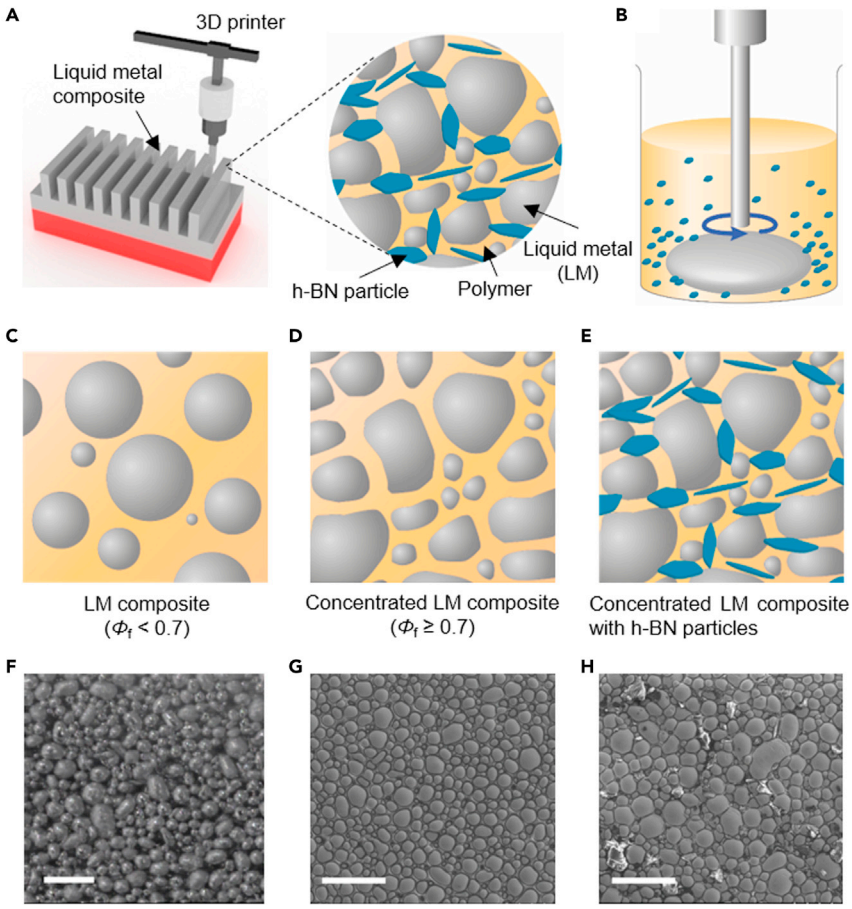

Figure 1. 3D printable LM composite with high thermal conductivity

(A–E) Schematic illustrations of (A) 3D printable LM composite and its internal structure, (B) LM composite preparation, (C) LM composite (Φ_{LM} < 0.7), (D) concentrated LM composite ($\Phi_{LM} \geq 0.7$), and (E) concentrated LM composite with h-BN particles.

(F) Microscopic image of the LM composite (Φ_{LM} = 0.5, the average size of LM droplets, d = 43.1 ± 21.7, Figure S1).

(G and H) SEM image of (G) concentrated LM compose (Φ_{LM} = 0.7, d = 38.2 ± 20.3) and (H) concentrated LM composite with h-BN particles (Φ_{LM} = 0.7, Φ_{BN} = 0.1, Φ_{BN} is the volume fraction of h-BN for the matrix, not whole composite, d = 40.4 ± 13.9). Scale bars = 200 μm.

gallium and indium was maintained, and it was found that the chemical state of the LM did not change during the dispersion process. Furthermore, the state of gallium and indium was remained even when h-BN particles were added to the LM composite, and as B-N peak (i.e., 190.1 eV) was detected in the B 1s spectra, we confirmed once again that the h-BN particles incorporated into the composite well. In addition, energy-dispersive X-ray spectroscopy (EDS) mapping confirmed spatially distribution of Ga, In, and h-BN for LM composite (Figures S5 and S6).

Thermal conductivity characterization

Before we discuss the experimental thermal conductivity of the concentrated LM composite, we theoretically determined the effect of the filler and polymer on the thermal conductivity of composite. Both the theoretical and experimental thermal conductivity described later in this paper mean isotropic thermal conductivity. The theoretical thermal conductivity was predicted using the Bruggeman formula, $1 - \Phi_f = \frac{k_c - k_f}{k_m - k_f}\left(\frac{k_m}{k_c}\right)^{\frac{1}{3}}$, where k_c, k_f, k_m are the thermal conductivity of the composite, filler, and matrix, and Φ_f is the volume fraction of the filler (Bruggeman, 1935). Figure 2A shows the prediction of k_c depending on k_m (0.1–0.3 W m^{-1} K^{-1}), and Figure 2B shows k_c depending on k_f (10, 30, and 100 W m^{-1} K^{-1}).

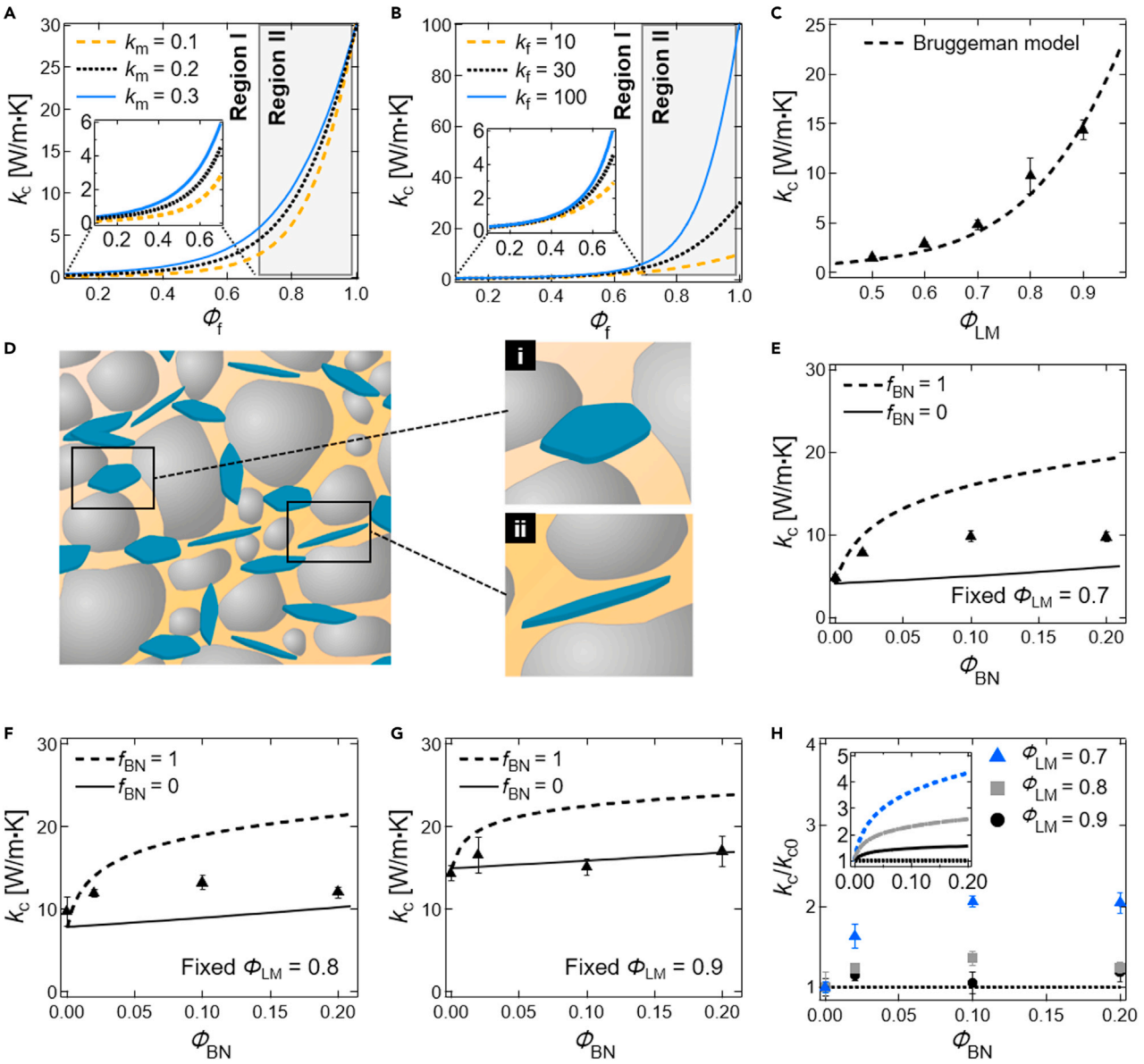

Figure 2. Thermal conductivity of the LM composite

(A and B) Theoretical k_c which is calculated from Bruggeman model as a function of the filler fraction (Φ_f) depending on the k of (A) the polymer matrix (k_m = 0.1, 0.2, 0.3 W m^{-1} K^{-1}, k_f = 30 W m^{-1} K^{-1}) and (B) the filler (k_f = 10, 30, 100 W m^{-1} K^{-1}, k_m = 0.2 W m^{-1} K^{-1}). Insets are the magnified graphs for region I.

(C) Experimental k_c of the LM composite as a function of Φ_{LM} (n = 3). The dashed line represents the theoretical k_c from the Bruggeman model.

(D) Schematic illustrations of h-BN which is placed between LM droplets. (i) h-BN makes direct heat paths between LM droplet. (ii) h-BN is just dispersed in the polymer matrix, not connecting heat path.

(E–G) Experimental k_c as a function of Φ_{BN} at a fixed Φ_{LM} = 0.7, 0.8, 0.9 in order, respectively (n = 3). Dashed line represents theoretical k_c where all h-BN added make heat paths between LM droplets (f_{BN} = 1), and the solid line is theoretical k_c where h-BN particles are just dispersed in the polymer, not connecting heat path (f_{BN} = 0).

(H) Normalized thermal conductivity (k_c/k_{c0}) as a function of Φ_{BN}, and k_{c0} is the experimental thermal conductivity of the LM composite at Φ_{BN} = 0.

For the composites, Φ_f = 0.5, k_c significantly increases to 0.766, 1.44, and 2.05, respectively, with an increasing k_m, whereas k_c did not change significantly to 1.19, 1.44, and 1.57, despite the larger increment of k_f. This means that k_c is dominantly affected k_m at low filler fractions (Φ_f < 0.7).

As the filler fraction of the composite has generally been under 0.7 due to the dispersion issue, processability, and the limit of the packing fraction, many studies have focused on enhancing k_m to achieve k_c (Akatsuka and

CellPress
OPEN ACCESS

Takezawa, 2003; Yoshihara et al., 2014). We refer the lower volume fractions ($\Phi_f < 0.7$) as region I, and the higher volume fractions ($\Phi_f \geq 0.7$) as region II. As shown in Figures 2A and 2B, k_f more effectively influences k_c than k_m for region II, and k_c approaches k_f regardless of k_m as expected. That means that a dramatically enhanced k_c could be achieved for $\Phi_f \geq 0.7$ because k_c in region II is close to k_f (30–320 W m^{-1} K^{-1}) (Hu et al., 2016; Xu and Chung, 2000), which is usually much higher than k_m (0.1–0.3 W m^{-1} K^{-1}) (Huang et al., 2011; Tanaka et al., 2012; Vadivelu et al., 2016). However, high k_c composites with >70 vol% have rarely been reported, presumably because it is extremely difficult to include more than 70 vol% of solid filler in the composite. Thus, we hypothesized that once we are able to create a composite in region II, k_c will be significantly improved.

To confirm our hypothesis, we made an LM composite ($\Phi_{LM} < 0.7$) and a concentrated LM composite ($\Phi_{LM} \geq 0.7$). Figure 2C shows that the experimental results (markers) are in good agreement with theoretical predictions (dotted line) obtained from the Bruggeman formula (Bruggeman, 1935). As predicted, a dramatically high k_c is achieved above $\Phi_{LM} = 0.7$, and k_c at $\Phi_{LM} = 0.9$ is 14.4 W m^{-1} K^{-1} which is roughly 10 times higher than k_c at $\Phi_{LM} = 0.5$.

A way to further improve thermal conductivity of the composite is to add high k particles in the polymeric matrix as the distance between LM droplets becomes small for high concentrations of LM composites. We chose electrically insulating h-BN (~30 μm, lateral dimension) as high k particles with anisotropic thermal conductivity (the planar direction: 200 W m^{-1} K^{-1}, the thickness direction: 2 W m^{-1} K^{-1}) (Tanimoto et al., 2013). Figure 1H is a SEM image of the concentrated LM composite made of an h-BN dispersed polymer matrix, and h-BN particles are located between the LM droplets. We hypothesized that h-BN particles exist in two types. As shown in Figure 2D i, h-BN particles can make a direct heat path between the LM droplets. Otherwise, h-BN particles are just dispersed in the polymer matrix without any connection (Figure 2D ii). If direct heat paths are created between LM droplets, it is expected that k_c is greatly enhanced, since rapid thermal conduction may be possible through high k particles without passing through a large heat resistant polymer.

To predict the effect of direct heat paths on k_c, we calculated theoretical k_c depending on the existence of heat paths (see STAR Methods for details). Φ_{BN} is the h-BN fraction for the matrix, and f_{BN} is the ratio of h-BN that makes a heat path to total input h-BN. As shown in Figure 2E, theoretical k_c at $\Phi_{BN} = 0.2$ is 4.4 times higher than that at $\Phi_{BN} = 0$ for the heat path connected system ($f_{BN} = 1$), whereas 1.5 times higher theoretical k_c at $\Phi_{BN} = 0.2$ is calculated for dispersed system ($f_{BN} = 0$). It should be noted that for a heat path connected system ($f_{BN} = 1$), even a small amount of h-BN ($\Phi_{BN} = 0.02$, 0.6 vol% h-BN for whole composite) can enhance theoretical k_c by 2.3 times. After the initial drastic k_c enhancement, k_c enhancement is relatively small, even if more h-BN particles are added (Figures 2E, 2F, and 2G). The experimental data are deviated from the solid line, if any heat path by h-BN is created.

The experimental data for the LM composites ($\Phi_{LM} = 0.7, 0.8$) are largely deviated from the theoretical prediction for dispersed system ($f_{BN} = 0$), whereas that of the LM composite ($\Phi_{LM} = 0.9$) almost follow the theoretical prediction of $f_{BN} = 0$ (Figures 2E, 2F, and 2G). At $\Phi_{LM} = 0.7, 0.8$, the deviation from the theoretical prediction ($f_{BN} = 0$) and drastic enhancement with a small amount of h-BN addition implies that heat paths are made between LM droplets. However, experimental data do not fully follow the theoretical prediction ($f_{BN} = 1$), but are placed between curves of $f_{BN} = 0$ and $f_{BN} = 1$, suggesting that h-BN exists as a mixture of both (one creating a heat path and the other being simply dispersed). Figures 2E and 2F also show that k_c enhancement is relatively small for $\Phi_{BN} > 0.1$ as predicted. Figure 2G shows k_c at fixed $\Phi_{LM} = 0.9$ increases from 14.1 W m^{-1}K^{-1} to 17.1 W m^{-1} K^{-1} by adding h-BN particles, but the k enhancement is not as large as that at lower Φ_{LM}. Figure 2H and the inset are experimental data and theoretical prediction for normalized thermal conductivity (k_c/k_{c0}) respectively. These indicate that this approach is more effective for enhancing k_c at a low Φ_{LM} for both experimental data and theoretical prediction. Especially for a 90 vol% LM composite with h-BN particles, an insufficient amount of polymer to fill the gap between LM droplets may suppress k enhancement. The size of h-BN used in the paper is ~30 μm, and k_c does not significantly increase with smaller particles (~1 μm, <150 nm). This may be because one large particle can create a heat path between LM droplets, whereas multiple particles are needed to make a path for smaller particles (Figure S7). A concentrated LM composite for a high k_c also exhibits an electrically insulating property at this high Φ_{LM} with and without h-BN (Figure S8 and STAR Methods for details).

Rheological property characterization

Before processing the LM composite, we characterized the rheological properties of the concentrated LM composite. As shown in Figures 3A–3D, concentrated LM composites ($\Phi_{LM} = 0.9$) exhibit crossover of

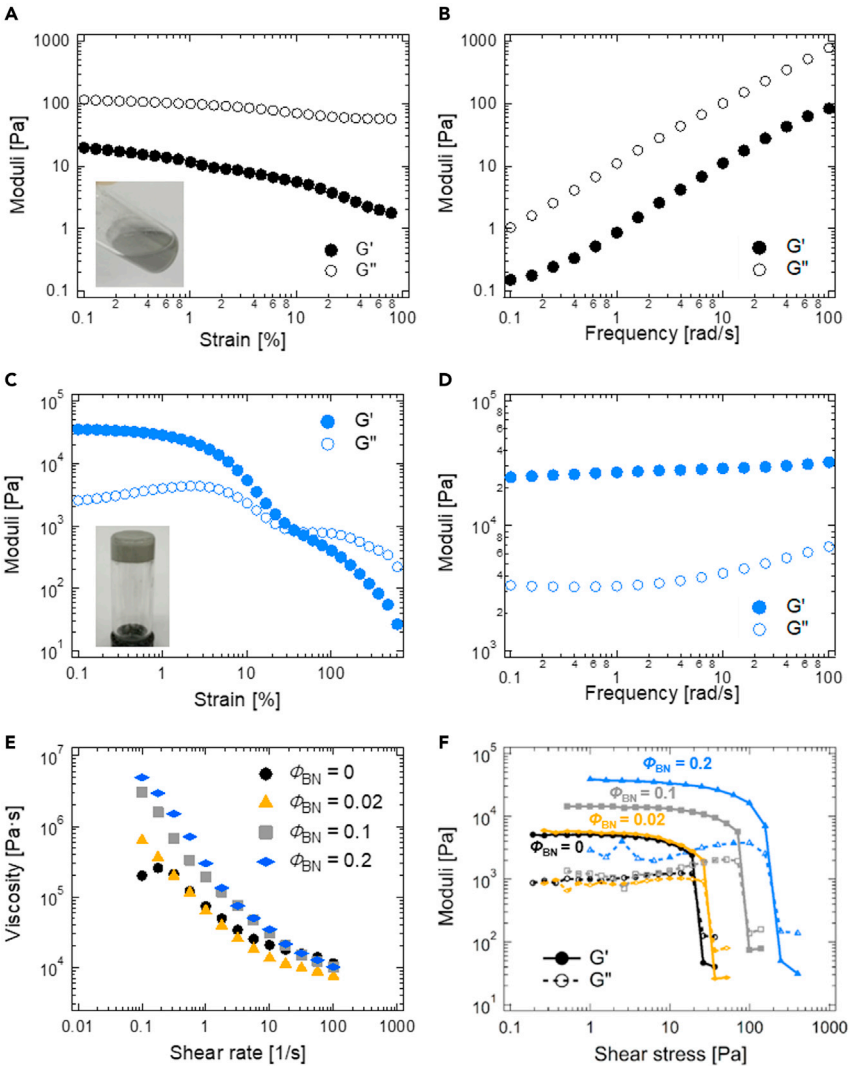

Figure 3. Rheology of LM composite

(A and B) (A) Amplitude sweep at a frequency of 10 rad/s (inset: photograph of flowing LM composite (Φ_{LM} = 0.5) when it is tilted), and (B) frequency sweep at strain of 1% for LM composite (Φ_{LM} = 0.5).

(C and D) (C) Amplitude sweep at a frequency of 10 rad/s (inset: photograph of non-flowing concentrated LM composite (Φ_{LM} = 0.9) when it is upside down) and (D) frequency sweep at strain of 1% for concentrated LM composite (Φ_{LM} = 0.9).

(E and F) (E) Viscosity as a function of shear rate and (F) storage and loss modulus as a function of shear stress for LM composite (Φ_{BN} = 0, 0.02, 0.1, 0.2 for polymer matrix, Φ_{LM} = 0.7 fixed).

storage modulus (G') and loss modulus (G'') at ~30% of strain and $G' > G''$ over the entire frequency range, which is unlike the LM composite (Φ_{LM} = 0.5). This indicates that the concentrated LM composite (Φ_{LM} = 0.9) maintains its shape at the bottom of the vial against gravity, whereas the LM composite (Φ_{LM} = 0.5) flows as nearly pure liquid (inset of Figures 3A and 3C). This implies that the 50 vol% LM composite can be extruded out from the nozzle for the 3D printer, but it spreads out after extruding and does not maintain its fiber shape. Additional LM to the 50 vol% LM composite serves as a rheology modifier to impart the essential rheological properties for 3D printing. As clogging generally occurs at this high filler fraction when the composite is used for the 3D printer, the rheological properties of the concentrated LM composites (Φ_{LM} = 0.7) with and without h-BN were also characterized. These composites exhibit viscoelastic properties similar to 90 vol% LM composites (Figure S9). As shown in Figure 3E, whereas the viscosity of LM composites (Φ_{LM} = 0.7) with and without h-BN increases with an increasing h-BN fraction, they exhibit shear thinning behavior in common which enables LM composites to be extruded through the nozzle under

modest printing pressure, and the viscosity (η) at a shear rate (0.7 s^{-1}), which was used for 3D printing in this study, is about 10^5–10^6 Pa·s. Figure 3F shows the plateau of G' and the yield shear stress at crossover points of G' and G'' increase with an increasing h-BN fraction, and they range from 10^3-10^5 Pa and 10^1–10^2 Pa, respectively. Thus, this sufficiently high G' and yield shear stress enable the LM composite to maintain the structure after extruding through the nozzle. All 70 vol% LM composites with and without h-BN readily extruded out from the nozzle and maintained the printed fiber shape, and we chose LM composite (Φ_{LM} = 0.7, Φ_{BN} = 0.2) as 3D printing ink which had a high yield stress which resisted the external force after 3D printing and a high k_c at the same time. In addition, the size of the droplets of concentrated LM composite was maintained even after one month (Figure S10).

Processing LM composite

The rheological properties of the LM composite are different depending on the LM and h-BN fraction, and the processing method varies accordingly. Low fraction LM composites (Φ_{LM} = 0.5) can be processed by molding, followed by UV curing (Figure 4A i). However, in this case, LM droplet sedimentation occurs at the bottom due to the density difference of the LM and polymer. The concentrated LM composite with h-BN (Φ_{LM} = 0.7, Φ_{BN} = 0.2) can be used as ink of a conventional 3D printer and make a fin structure with about a 820 μm thickness (Figure 4A ii). At a high fraction (Φ_{LM} = 0.9), it is difficult to 3D print the LM composite in a desired shape due to clogging and an uncontrollable extrusion rate with a 410 μm sized nozzle but can be easily processed by molding and extrusion with a syringe (Figure 4A iii).

Figure 4B is the SEM image of the extruded fiber through the nozzle (410 μm) of the 3D printer showing that LM exists as droplets with a maintained internal structure of the concentrated LM composite. The size of LM droplet before and after 3D printing is almost the same (Figure S11). Figure 4C shows a sequential snapshot of a video clip of producing a fin structure using a 3D printer with a nozzle size of 410 μm—minimum size used for 3D printing in this paper (Video S1). The thickness of the extruded fin is about 820 μm, and the height is about 4 mm. Layers of the 3D printed fin is shown in Figure 4D, showing that the thickness of each layer of the fin are nearly the same. Furthermore, we created a structure such as a lattice structure that is difficult to be processed by molding. Figure 4E shows the lattice structure made of the LM composite using a 3D printer (Video S2). As this structure has a surface area that exceeds the existing limited surface area of the composite, it can influence the enhancement of the heat dissipation rate.

Heat dissipation of LM composite

To demonstrate the actual heat dissipation effect of the LM composite, the heat dissipation of LM composites (Φ_{LM} = 0.7, Φ_{BN} = 0.2) depending on structures (lattice structure and simple cuboid) are recorded using an IR camera after heating them with a heat gun (setting temperature: 573 K) for 100 s (Video S3). The width, length, and height of the structure are identical for the two structures, since the assigned space for heat dissipating materials is limited for practical applications. As shown in Figure 5A, the lattice structure exhibits faster heat dissipation than a cuboid structure. The temperature at the top surface (T_{sur}) increases and decreases faster for the lattice structure, and the maximum temperature differences between the two structures during heat dissipation is about 6.4 K (Figure S12). However, the difference in T_{sur} between the two structures alone cannot fully explain the actual heat dissipation depending on the structures because it does not take into account the difference in volume for each structure, resulting in the difference in stored heat, Q (J). To consider the difference in volume and get more information other than T_{sur}, we numerically calculated the heat dissipation of these two structures using finite element method (FEM) simulation (Figure 5B, see details in Figures S13–S17 and STAR Methods for details). The exact heat is calculated and normalized, determining the normalized heat dissipation $\left(X_h, X_h = \frac{Q(t)-Q_0}{Q_{max}-Q_0}\right)$; the heat increment ($Q(t) - Q_0$) is divided by the maximum heat difference ($Q_{max} - Q_0$). From the temporal change of X_h and X_c (= 1 − X_h), it is found that the lattice structure dissipates heat 20% faster than the cuboid in early stages of heat dissipation (Figure 5B and inset). In practical heat dissipation, the rate of heat dissipation is influenced not only by the surface area but also by the heat transfer coefficient. As a result of the simulation, the heat transfer coefficient of the lattice structure (h') is 1/5 of that of the cuboid (h), and this difference may be due to the narrow distance between the fibers, partially clogged holes due to the limit of 3D printing for the lattice structure and weak convection using a small fan (Table S1). If the heat transfer coefficient of the lattice structure is equal to that of the cuboid with strong convection, the heat dissipation rate can be largely improved (dotted line in Figure 5B and inset). In short, the heat dissipation rate of lattice structure is

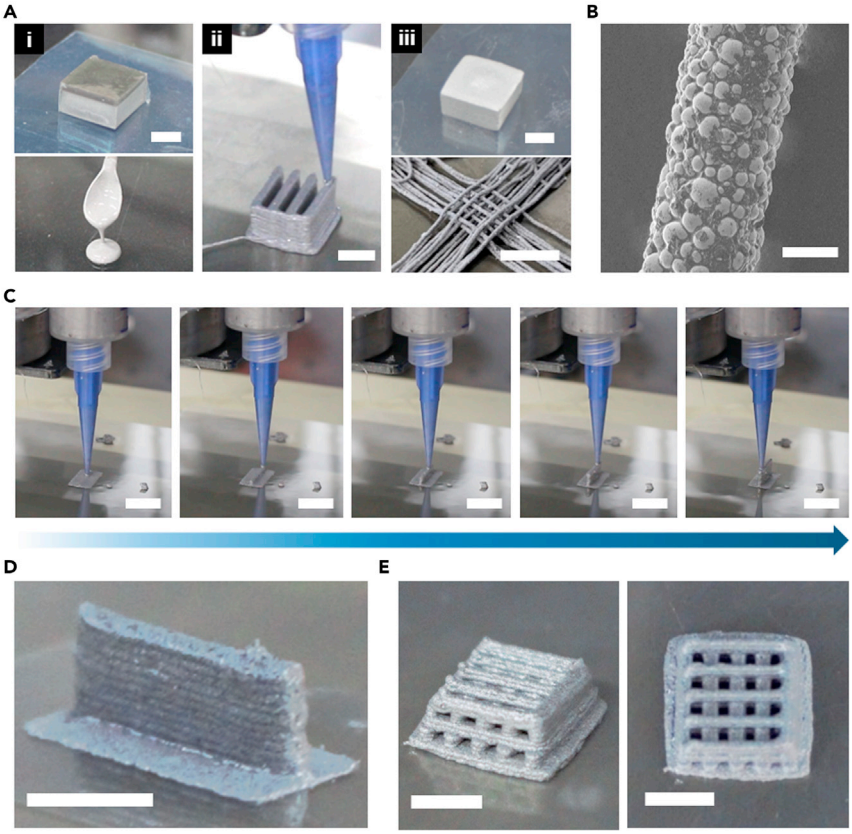

Figure 4. Processable LM composite

(A) Different processability depending on Φ_{LM}. i. LM composite (Φ_{LM} = 0.5). Cured cuboid structure and flowing property. ii. Concentrated LM composite (Φ_{LM} = 0.7, Φ_{BN} = 0.2) 3D printed. iii. Concentrated LM composite (Φ_{LM} = 0.9). Uncured cuboid structure and lattice structure processed by extrusion with a syringe (scale bars = 5 mm).

(B) SEM image of the fiber (Φ_{LM} = 0.7, Φ_{BN} = 0.2) extruded through the nozzle (scale bar = 200 μm).

(C) Sequential snapshots for 3D printing of the fin structure. A concentrated LM composite (Φ_{LM} = 0.7, Φ_{BN} = 0.2) was used. Chunks of the LM composite placed to the right of the fin structure were dropped from nozzle before 3D printing (scale bar = 5 mm).

(D) Layers of a 3D printed fin structure. Spike at the top is the mark made by the nozzle removed after 3D printing.

(E) 3D printed lattice structure (scale bars = 5 mm).

higher than that of the cuboid in spite of a low heat transfer coefficient, and in a strong convection system, a lattice structure can dramatically enhance the rate of heat dissipation.

CONCLUSIONS

Here, we demonstrated 3D printable concentrated LM composites with high thermal conductivity that overcame the trade-off relation between a high k and processability in the conventional heat dissipation composite. Thermal conductivity of the LM composite was significantly increased by changing the LM fraction from the conventionally used matrix dominant region ($\Phi_{LM} < 0.7$) to the filler dominant region ($\Phi_{LM} \geq 0.7$). Through this strategy, we achieved about a 10 times higher k_c (14.4 W m^{-1} K^{-1}) for the concentrated LM composite (Φ_{LM} = 0.9) than that for the LM composite (Φ_{LM} = 0.5), whereas the composite containing 63.8 vol% Al_2O_3 (~k of LM) was 2.68 W m^{-1} K^{-1} (Huang et al., 2011; Nagai and Lai, 1997). Moreover, by adding 3 vol% of h-BN in a concentrated LM composite, k_c was enhanced by two times at a fixed Φ_{LM} = 0.7, and the maximum k_c (Φ_{LM} = 0.9, Φ_{BN} = 0.2) was 17.1 W m^{-1} K^{-1}, which is >70% higher than k_c for LM polymeric composites reported in the previous research. The concentrated LM composite for enhancing k_c also exhibited a shear thinning behavior and suitable yield stress, so we could use it as an ink for conventional 3D printer and make a lattice structure that cannot be made by molding. This exceptional combination of high thermal conductivity and 3D printable rheological properties not only provide on-demand processing of

CellPress
OPEN ACCESS

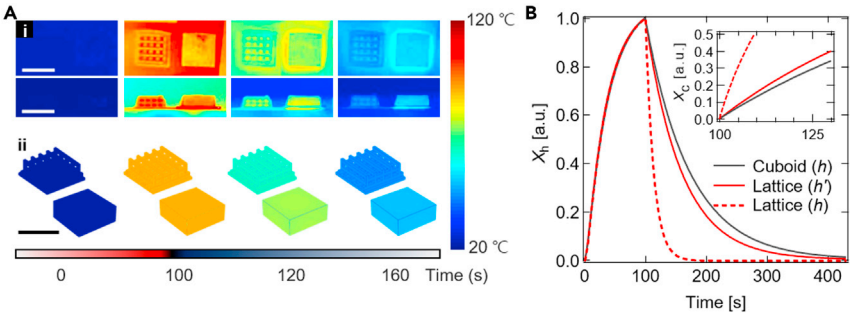

Figure 5. Heat dissipation of a lattice structure and simple cuboid

(A) IR camera observation and COMSOL simulation. i. Sequential snapshots for IR camera observation of the lattice structure and simple cuboid made of the LM composite (Φ_{LM} = 0.7, Φ_{BN} = 0.2) after applying heat for 100 s using a heat gun (setting temperature: 573 K). Temperatures in the current image are for LM composites only and emissivity corrections are required to read temperatures other than LM composites. ii. Corresponding snapshots of numerical simulation through T_{sur} fitting.

(B) Normalized heat dissipation (X_h) as a function of time. (inset: $X_c = 1 - X_h$, the degree of cooling as a function of time). Each h and h' are the heat transfer coefficient for the heat dissipation (cooling) for the simple cuboid and lattice structure ($h > h'$). Scale bars = 1 cm.

the desired structures for heat dissipation materials under ambient conditions, but it also leads to rapid heat dissipation by increasing the surface area. This unique combination shows the great potential to enable developments for various types/forms of heat dissipation materials that cannot be made by molding, pressing, and cutting, and opening for a new type of device design. This may suggest more technological opportunities for LM composite design and lead to a new horizon for LM research.

Limitations of study

In this research, we fabricated the high heat dissipation material that show both high thermal conductivity and excellent processability using liquid filler. The fraction capable of 3D printing without clogging was Φ_{LM} = 0.7 and Φ_{BN} = 0.2 (the nozzle size: 410 μm). For fractions above that (e.g., Φ_{LM} = 0.9), processing was performed only by molding due to clogging.

STAR★METHODS

Detailed methods are provided in the online version of this paper and include the following:

- KEY RESOURCES TABLE
- RESOURCE AVAILABILITY
  - Lead contact
  - Materials availability
  - Data and code availability
- METHOD DETAILS
  - LM composite preparation
  - Thermal characterization
  - Characterization of chemical state of pure LM, LM composite, and LM composite with h-BN particles
  - EDS mapping
  - Characterization of internal structure using X-ray microscope
  - 3D printing preparation
  - Rheological characterization
  - IR observation
  - Theoretical prediction of thermal conductivity
  - Electrical characterization
  - Numerical details of time dependent heat simulation

SUPPLEMENTAL INFORMATION

Supplemental information can be found online at https://doi.org/10.1016/j.isci.2021.103183.

ACKNOWLEDGMENTS

This work was supported by LG Chem (project number: G01160132) and the Basic Science Research Program through the National Research Foundation of Korea (grant number: 2021R1A2C2009859).

AUTHOR CONTRIBUTIONS

S.M. and S.Q.C. conceptualized the idea and designed the experiments. S.M. performed the central experiments and analysis. H.K. conducted numerical simulations for the heat dissipation. S.M. and K.L. fabricated the structure using 3D printer. S.M. and J.P. performed IR observation for the heat dissipation. Y.K. discussed and commented on the concept and methodology. All authors discussed the results and commented on the manuscript.

DECLARATION OF INTERESTS

The authors declare no competing interests.

Received: June 8, 2021
Revised: August 17, 2021
Accepted: September 23, 2021
Published: October 22, 2021

SUPPORTING CITATIONS

The following references appear in the Supplemental information: Ishida and Rimdusit, 1999.

REFERENCES

Akatsuka, M., and Takezawa, Y. (2003). Study of high thermal conductive epoxy resins containing controlled high-order structures. J. Appl. Polym. Sci. *89*, 2464–2467.

Bartlett, M.D., Kazem, N., Powell-Palm, M.J., Huang, X., Sun, W., Malen, J.A., and Majidi, C. (2017). High thermal conductivity in soft elastomers with elongated liquid metal inclusions. Proc. Natl. Acad. Sci. *114*, 2143–2148.

Biercuk, M.J., Llaguno, M.C., Radosavljevic, M., Hyun, J.K., Johnson, A.T., and Fischer, J.E. (2002). Carbon nanotube composites for thermal management. Appl. Phys. Lett. *80*, 2767–2769.

Blaiszik, B.J., Kramer, S.L.B., Grady, M.E., McIlroy, D.A., Moore, J.S., Sottos, N.R., and White, S.R. (2012). Autonomic restoration of electrical conductivity. Adv. Mater. *24*, 398–401.

Boudenne, A., Ibos, L., Fois, M., Majesté, J.C., and Géhin, E. (2005). Electrical and thermal behavior of polypropylene filled with copper particles. Compos. Part A Appl. Sci. Manuf. *36*, 1545–1554.

Bruggeman, D. (1935). Berechnung verschiedener physikalischer Konstanten von heterogenen Substanzen. I. Dielektrizitätskonstanten und Leitfähigkeiten der Mischkörper aus isotropen Substanzen.No Title. Ann. Phys. *416*, 636–664.

Chang, C.W., Fennimore, A.M., Afanasiev, A., Okawa, D., Ikuno, T., Garcia, H., Li, D., Majumdar, A., and Zettl, A. (2006). Isotope effect on the thermal conductivity of boron nitride nanotubes. Phys. Rev. Lett. *97*, 1–4.

Chung, S., Lee, J.H., Jeong, J., Kim, J.J., and Hong, Y. (2009). Substrate thermal conductivity effect on heat dissipation and lifetime improvement of organic light-emitting diodes. Appl. Phys. Lett. *94*, 65–68.

Cinchetti, M., Dediu, V.A., and Hueso, L.E. (2017). Activating the molecular spinterface. Nat. Mater. *16*, 507–515.

Deng, Y., and Liu, J. (2010). A liquid metal cooling system for the thermal management of high power LEDs. Int. Commun. Heat Mass Transf. *37*, 788–791.

Dickey, M.D. (2014). Emerging applications of liquid metals featuring surface oxides. ACS Appl. Mater. Interfaces *6*, 18369–18379.

Fassler, A., and Majidi, C. (2015). Liquid-phase metal inclusions for a conductive polymer composite. Adv. Mater. *27*, 1928–1932.

Hu, Y., Du, G., and Chen, N. (2016). A novel approach for Al_2O_3/epoxy composites with high strength and thermal conductivity. Compos. Sci. Technol. *124*, 36–43.

Huang, X., Jiang, P., and Tanaka, T. (2011). A review of dielectric polymer composites with high thermal conductivity. IEEE Electr. Insul. Mag. *27*, 8–16.

Ishida, H., and Rimdusit, S. (1998). Very high thermal conductivity obtained by boron nitride-filled polybenzoxazine. Thermochim. Acta *320*, 177–186.

Ishida, H., and Rimdusit, S. (1999). Heat capacity measurement of boron nitride-filled polybenzoxazine. The composite structure-insensitive property. J. Therm. Anal. Calorim. *58*, 497–507.

Jeong, S.H., Chen, S., Huo, J., Gamstedt, E.K., Liu, J., Zhang, S.L., Zhang, Z. Bin, Hjort, K., and Wu, Z. (2015). Mechanically stretchable and electrically insulating thermal elastomer composite by liquid alloy droplet embedment. Sci. Rep. *5*, 1–10.

Khan, M.R., Eaker, C.B., Bowden, E.F., and Dickey, M.D. (2014a). Giant and switchable surface activity of liquid metal via surface oxidation. Proc. Natl. Acad. Sci. U. S. A. *111*, 14047–14051.

Khan, M.R., Trlica, C., So, J.H., Valeri, M., and Dickey, M.D. (2014b). Influence of water on the interfacial behavior of gallium liquid metal alloys. ACS Appl. Mater. Interfaces *6*, 22467–22473.

Kumlutaş, D., Tavman, I.H., and Turhan Çoban, M. (2003). Thermal conductivity of particle filled polyethylene composite materials. Compos. Sci. Technol. *63*, 113–117.

Ladd, C., So, J.H., Muth, J., and Dickey, M.D. (2013). 3D printing of free standing liquid metal microstructures. Adv. Mater. *25*, 5081–5085.

Lin, Y., Cooper, C., Wang, M., Adams, J.J., Genzer, J., and Dickey, M.D. (2015). Handwritten, soft circuit boards and antennas using liquid metal nanoparticles. Small *11*, 6397–6403.

Lin, Y., Gordon, O., Khan, M.R., Vasquez, N., Genzer, J., and Dickey, M.D. (2017). Vacuum filling of complex microchannels with liquid metal. Lab Chip *17*, 3043–3050.

Liu, C.H., Huang, H., Wu, Y., and Fan, S.S. (2004). Thermal conductivity improvement of silicone elastomer with carbon nanotube loading. Appl. Phys. Lett. *84*, 4248–4250.

Ma, K.Q., and Liu, J. (2007). Heat-driven liquid metal cooling device for the thermal management of a computer chip. J. Phys. D Appl. Phys. *40*, 4722–4729.

Markvicka, E.J., Bartlett, M.D., Huang, X., and Majidi, C. (2018). An autonomously electrically self-healing liquid metal–elastomer composite for robust soft-matter robotics and electronics. Nat. Mater. *17*, 1–7.

Mei, S., Gao, Y., Deng, Z., and Liu, J. (2014). Thermally conductive and highly electrically resistive grease through homogeneously dispersing liquid metal droplets inside methyl silicone oil. J. Electron. Packag. Trans. ASME *136*, 1–7.

Mineart, K.P., Lin, Y., Desai, S.C., Krishnan, A.S., Spontak, R.J., and Dickey, M.D. (2013). Ultrastretchable, cyclable and recyclable 1- and 2-dimensional conductors based on physically cross-linked thermoplastic elastomer gels. Soft Matter *9*, 7695–7700.

Nagai, Y., and Lai, G.C. (1997). Thermal conductivity of epoxy resin filled with particulate aluminum nitride powder. J. Ceram. Soc. Jpn. *105*, 197–200.

Neumann, T.V., and Dickey, M.D. (2020). Liquid metal direct write and 3D printing: a review. Adv. Mater. Technol. *2000070*, 1–16.

Neumann, T.V., Facchine, E.G., Leonardo, B., Khan, S., and Dickey, M.D. (2020). Direct write printing of a self-encapsulating liquid metal-silicone composite. Soft Matter *16*, 6608.

Ohashi, M., Kawakami, S., Yokogawa, Y., and Lai, G.C. (2005). Spherical aluminum nitride fillers for heat-conducting plastic packages. J. Am. Ceram. Soc. *88*, 2615–2618.

Palleau, E., Reece, S., Desai, S.C., Smith, M.E., and Dickey, M.D. (2013). Self-healing stretchable wires for reconfigurable circuit wiring and 3D microfluidics. Adv. Mater. *25*, 1589–1592.

Park, S., Baugh, N., Shah, H.K., Parekh, D.P., Joshipura, I.D., and Dickey, M.D. (2019a). Ultrastretchable elastic shape memory fibers with electrical conductivity. Adv. Sci. *6*, 1901579.

Park, Y.G., Min, H., Kim, H., Zhexembekova, A., Lee, C.Y., and Park, J.U. (2019b). Three-dimensional, high-resolution printing of carbon nanotube/liquid metal composites with mechanical and electrical reinforcement. Nano Lett. *19*, 4866–4872.

Rahim, M.A., Centurion, F., Han, J., Abbasi, R., Mayyas, M., Sun, J., Christoe, M.J., Esrafilzadeh, D., Allioux, F.M., Ghasemian, M.B., et al. (2021). Polyphenol-induced adhesive liquid metal inks for substrate-independent direct pen writing. Adv. Funct. Mater. *31*, 2007336.

Saborio, M.G., Cai, S., Tang, J., Ghasemian, M.B., Mayyas, M., Han, J., Christoe, M.J., Peng, S., Koshy, P., Esrafilzadeh, D., et al. (2020). Liquid metal droplet and graphene co-fillers for electrically conductive flexible composites. Small *16*, 1–12.

Tanaka, T., Kozako, M., and Okamoto, K. (2012). Toward high thermal conductivity nano micro epoxy composites with sufficient endurance voltage. J. Int. Counc. Electr. Eng. *2*, 90–98.

Tang, L., Mou, L., Zhang, W., and Jiang, X. (2019). Large-scale fabrication of highly elastic conductors on a broad range of surfaces. ACS Appl. Mater. Interfaces *11*, 7138–7147.

Tanimoto, M., Yamagata, T., Miyata, K., and Ando, S. (2013). Anisotropic thermal diffusivity of hexagonal boron nitride-filled polyimide films: effects of filler particle size, aggregation, orientation, and polymer chain rigidity. ACS Appl. Mater. Interfaces *5*, 4374–4382.

Teng, C.C., Ma, C.C.M., Lu, C.H., Yang, S.Y., Lee, S.H., Hsiao, M.C., Yen, M.Y., Chiou, K.C., and Lee, T.M. (2011). Thermal conductivity and structure of non-covalent functionalized graphene/epoxy composites. Carbon *49*, 5107–5116.

Vadivelu, M.A., Kumar, C.R., and Joshi, G.M. (2016). Polymer composites for thermal management: a review. Compos. Interfaces *23*, 847–872.

Wang, L., and Liu, J. (2014). Compatible hybrid 3D printing of metal and nonmetal inks for direct manufacture of end functional devices. Sci. China Technol. Sci. *57*, 2089–2095.

Wissman, J., Dickey, M.D., and Majidi, C. (2017). Field-controlled electrical switch with liquid metal. Adv. Sci. *4*, 1700169.

Xin, Y., Peng, H., Xu, J., and Zhang, J. (2019). Ultrauniform embedded liquid metal in sulfur polymers for recyclable, conductive, and self-healable materials. Adv. Funct. Mater. *29*, 1–7.

Xu, Y., Chung, D.D.L., and Mroz, C. (2001). Thermally conducting aluminum nitride polymer matrix composites. Compos. Pt. A-Appl. S *32*, 1749–1757.

Xu, Yunsheng, and Chung, D.D.L. (2000). Increasing the thermal conductivity of boron nitride and aluminum nitride particle epoxy-matrix composites by particle surface treatments. Compos. Interfaces *7*, 243–256.

Yang, D., Yao, Q., Jia, M., Wang, J., Zhang, L., Xu, Y., and Qu, X. (2021). Application analysis of efficient heat dissipation of electronic equipment based on flexible nanocomposites. Energy Built Environ. *2*, 157–166.

Yang, X.H., and Liu, J. (2018). Liquid metal enabled combinatorial heat transfer science: toward unconventional extreme cooling. Front. Energy *12*, 259–275.

Yoshihara, S., Tokita, M., Ezaki, T., Nakamura, M., Sakaguchi, M., Matsumoto, K., and Watanabe, J. (2014). Main-chain smectic liquid crystalline polymer exhibiting unusually high thermal conductivity in an isotropic composite. J. Appl. Polym. Sci. *131*, 1–5.

Yu, S., and Kaviany, M. (2014). Electrical, thermal, and species transport properties of liquid eutectic Ga–In and Ga–In-Sn from first principles. J. Chem. Phys. *140*, 1–8.

Yung, K.C., and Liem, H. (2013). Enhanced thermal conductivity of boron nitride epoxy-matrix composite through multi-modal particle size mixing. J. Appl. Polym. Sci. *21*, 449–456.

Zhou, S.-Q., and Ni, R. (2008). Measurement of the specific heat capacity of water-based Al_2O_3 nanofluid. Appl. Phys. Lett. *92*, 093123.

Zhou, W., Qi, S., Li, H., and Shao, S. (2007). Study on insulating thermal conductive BN/HDPE composites. Thermochim. Acta *452*, 36–42.

Zhu, J.Y., Tang, S.Y., Khoshmanesh, K., and Ghorbani, K. (2016). An integrated liquid cooling system based on galinstan liquid metal droplets. ACS Appl. Mater. Interfaces *8*, 2173–2180.

Zhu, S., So, J.H., Mays, R., Desai, S., Barnes, W.R., Pourdeyhimi, B., and Dickey, M.D. (2013). Ultrastretchable fibers with metallic conductivity using a liquid metal alloy core. Adv. Funct. Mater. *23*, 2308–2314.

STAR★METHODS

KEY RESOURCES TABLE

REAGENT or RESOURCE	SOURCE	IDENTIFIER
Chemicals, peptides, and recombinant proteins		
EGaIn	Sigma Aldrich	Cat#495425
Liquid photopolymer	Norland Products, Inc.	NOA 68
h-BN	DENKA	XGP; CAS 10043-11-5
Acetone	OCI	CAS: 67-64-1
Software and algorithms		
COMSOL	COMSOL Inc.	https://www.comsol.com/
MATLAB	MathWorks	https://www.mathworks.com/

RESOURCE AVAILABILITY

Lead contact

Further information and requests for resources and reagents should be directed and will be fulfilled by the lead contact, Siyoung Q. Choi (sqchoi@kaist.ac.kr).

Materials availability

This study did not generate new unique reagents.

Data and code availability

- Original data reported in this paper will be shared by the lead contact upon request.
- This paper does not report original code.
- Any additional information required to reanalyze the data reported in this paper is available from the lead contact upon request.

METHOD DETAILS

LM composite preparation

Before preparation of the LM composites, acetone (99.8%, OCI) was added to uncured NOA 68 (1 ml, Norland Products, Inc.) to lower the viscosity of the polymer matrix (1 ml, acetone:uncured NOA 68 = 1:1 by volume). For the preparation of the LM composite with h-BN, the amount of acetone was equal to the sum of h-BN and NOA 68 by volume. h-BN (99%, XGP, DENKA) which is plate-shaped particles with an average lateral size of 30 μm were added to polymer mixture so that Φ_{BN} = 0.02, 0.1, 0.2 for the total matrix excluding acetone, respectively. These mixtures were then subjected to a vortex mixer (VM-10, DAIHAN Scientific) for 1 min at 3,000 rpm and to the bath sonicator (WUC-D06H, Wisd.) for 30 minutes at 298 K.

As shown in Figure 1B, the LM composite was prepared by breaking up EGaIn (500 μL to 900 μL, 75.5 wt% Ga, 24.5 wt%, Sigma Aldrich) in the prepared mixture, while varying Φ_{LM} from 0.5 to 0.9 by increments of 0.1. Acetone was not included in the Φ_{LM} calculation, because it was removed in the final step. The LM composite ($\Phi_{LM} < 0.8$) was prepared by adding the desired EGaIn at once and breaking EGaIn in a number of droplets with the vortex mixer at 3,000 rpm for 30 s and a homogenizer with 20,000 rpm for 30 s. For the LM composite with a higher fraction ($\Phi_{LM} \geq 0.8$), a half of EGaIn was added to the prepared polymer matrix and was then subjected to the vortexing mixer for 30 s at 3,000 rpm. After repeating this process with the rest of EGaIn, the LM composite was subjected to the homogenizer for 1 min at 20,000 rpm. The resulting LM composite was placed in a fume hood and the vial lid was left open for 12 hours to evaporate the acetone in the LM composite. To ensure that there was no residual solvent, the LM composite was put in the vacuum conditions for 5 min using a vacuum oven (OV-11, JEIO TECH) prior to sampling for thermal conductivity measurements and 3D printing. If air bubbles were found in the LM composite under vacuum conditions, the putting and evaporating of solvent processes were repeated.

CellPress
OPEN ACCESS

Thermal characterization

Thermal conductivity was not directly measured, but was calculated from the following formula, $k = \alpha C_p \rho$, where α is the thermal diffusivity measured using a laser flash apparatus (LFA 447, NETZSCH), C_p is the calculated specific heat capacity, and ρ is the calculated density (Figure S18; Table S2). All the measurements were conducted at 298 K. Uncured LM composites (Φ_{LM} = 0.5 to 0.9) with and without h-BN were loaded in aluminum holders and then cured upon exposure to UV light for 10 min in a cure box (Raynics). After that, the surface of the LM composite was cured, so it was not smeared for any measurements. The diffusivity of the LM composites was analyzed by a 2-layers diffusivity model with a known value for aluminum (α, C_p, ρ, and thickness) and LM composites (C_p, ρ, and thickness) in the LFA analysis program (Proteus LFA Analysis, NETZSCH). The thickness of the LM sample was determined by subtracting the thickness of the aluminum holder from the total thickness of the holder containing the cured LM composite, and the thickness was measured using litematic (VL-50A, Miutoyo). C_p of the LM composites was calculated from the following formula $C_p = C_{p,\,LM}F_{LM} + C_{p,NOA}F_{NOA}$, where $C_{p,LM}$, $C_{p,NOA}$ were the measured specific heat capacity of LM, NOA 68 (Table S2) using ultra low temp differential scanning calorimetry (DSC 214 Polyma, NETZSCH) and modulated differential scanning calorimeter (DSC204 F1 Phoenix, NETZSCH), and F_{LM}, F_{NOA} are the mass fraction of LM and NOA 68 (Zhou and Ni, 2008). ρ of LM composites is calculated from the following formula, $\rho = \rho_{LM}\Phi_{LM} + \rho_{NOA}\Phi_{NOA}$, where ρ_{LM}, ρ_{NOA} are the density of LM, NOA 68 (Table S2), and $\Phi_{LM,}$ Φ_{NOA} are the volume fraction of LM, NOA 68.

Characterization of chemical state of pure LM, LM composite, and LM composite with h-BN particles

The chemical distributions were also measured by using XPS [Thermo VG Scientific Sigma Probe system equipped with an Al Kα X-ray source (1486.6 eV)] with an energy resolution of 0.47 eV full width at half maximum under ultra-high vacuum conditions (below 10^{-9} Torr). The core level of each photoelectron spectra was calibrated by adventitious carbon peak (*i.e.* the C 1s core-level peak to 284.8 eV). The samples were drop-casted on Si water and then acetone was dropped on the samples to desorb top polymer layer of the samples.

EDS mapping

EDS mapping were obtained using Schottky Field Emission Scanning Electron Microscope (SU5000, Hitachi) operated at 15 kV. The samples were drop-casted on conductive carbon adhesive tapes and then acetone was dropped on the samples to desorb top polymer layer of the samples.

Characterization of internal structure using X-ray microscope

Cross-sectional view of the concentrated LM composite was obtained using X-ray microscope (ZEISS Xradia 520 Versa). Samples were prepared in 4ml vials without curing.

3D printing preparation

3D printing of the LM concentrated composite (Φ_{LM} = 0.7, Φ_{BN} = 0.2) was conducted with a custom-built strain control 3D printer (pinter334, Samdimall) based on a Cartesian geometry system with a 410 μm nozzle tip (7018298, Nordson EFD). All print paths were generated by writing the appropriate G-code commands (Cura). The lattice structure was printed at 1mm/s with a strain rate 0.7 s^{-1} under ambient conditions. After 3D printing, the printed LM composite was cured upon exposure to UV light for 10 min in a cure box (Raynics).

Rheological characterization

Rheological characterizations of the LM composite were conducted under ambient conditions using a rheometer (MCR-302, Anton Paar), equipped with a 25 mm parallel-plate geometry (PP25/S, Anton Paar). The gap distance was 1 mm for all LM composites. Prior to the characterization, all LM composites were prepared in the same way with preparation for 3D printing and cautiously transferred to the lower plate of the rheometer using a spatula. All LM composites were uncured. To characterize rheological properties related to 3D printing, an amplitude sweep at 10 rad/s, frequency sweep at 1% strain, and viscometry measurements were carried out for the LM composites (Φ_{LM} = 0.7, Φ_{BN} = 0, 0.02, 0.1, 0.2).

IR observation

To test the actual heat dissipation according to the structures, the heating and cooling (heat dissipation) steps were performed with an LM concentrated composite (Φ_{LM} = 0.7, Φ_{BN} = 0.2) of a lattice structure and a simple

cuboid. Each of them was processed by 3D printing and molding. To track the temperature change, a FLIR A325sc camera with the corrected emissivity value for the LM composite was used. All the videos were recorded 20 cm above the samples. The materials were located on fluorinated ethylene propylene polymer films and the films were located on a flat poly(styrene) dish. The samples were first heated with a heat gun (Bosch 630 DCE) with a set temperature of 573 K for 100 s held at the top of the sample. The distance between the gun and the samples was about 20 cm. After the heating process, a fan was located 20 cm above the samples right next to the IR camera, providing 2.5 m/s convective air flow for cooling. The cooling process was continued until the temperature of the samples nearly reached the atmospheric temperature. For the heat dissipation analysis, all the experimental conditions containing the distance between the camera and sample, the emissivity of sample, the values of relative humidity, and ambient air temperature were applied for recorded videos through the FLIR Tools program. The emissivity value of the sample was 0.695, the relative humidity was about 15%, and the average ambient temperature was about 295 K. Each video for the top and side view was recorded separately. For further comparison with the numerical simulation results, grayscale images displaying surface temperatures from 293 K to 393 K were recorded as videos. In a MATLAB environment, the temperature was averaged at the top surface for each time step and each structure (see Numerical details of time dependent heat simulation in STAR Methods for details).

Theoretical prediction of thermal conductivity

As shown in Figure 2C, the measured thermal conductivity is in good agreement with predictions obtained from the Bruggeman formulation that was adapted to predict the bulk thermal conductivity for the composite system as a function of Φ_f, the filler volume fraction.

$$1 - \Phi_f = \frac{k_c - k_f}{k_m - k_f}\left(\frac{k_m}{k_c}\right)^{\frac{1}{3}} \quad \text{(Equation 1)}$$

where k_c, k_f, and k_m are the thermal conductivity of composite, filler, and matrix (Bruggeman, 1935).

To account for the k enhancement effect according to the addition of h-BN particles, we additionally calculated k_m with and without creating heat paths. When added h-BN particles did not create any heat path between LM droplets, the h-BN in polymer matrix was another composite system like the LM composite. k_m can be also calculated from applying the Bruggeman formula.

$$1 - \Phi_{BN} = \frac{k_m - k_{BN}}{k_{NOA} - k_{BN}}\left(\frac{k_{NOA}}{k_m}\right)^{\frac{1}{3}} \quad \text{(Equation 2)}$$

where k_m, k_{BN}, and k_{NOA} are the thermal conductivity of matrix, h-BN, and NOA 68 polymer, and Φ_{BN} is the h-BN fraction for the matrix (Bruggeman, 1935).

Otherwise, when heat paths are created in the LM composite, h-BN particles come into contact with the LM droplets (Figure 2D i). For simplicity, we assumed that h-BN and the polymer are placed in parallel between LM droplets and k_m is calculated from the parallel model,

$$k_m = k_{BN}\Phi_{BN} + k_{NOA}(1 - \Phi_{BN}) \quad \text{(Equation 3)}$$

By substituting k_m calculated from the two models in Equation (1), the values of thermal conductivity with and without creating a heat path were roughly predicted.

k_{NOA} is 0.175 W m^{-1} K^{-1} which is the measured value and k_{BN} for predicting theoretical k_c is 40 W m^{-1} K^{-1}, not considering anisotropy of h-BN.

Electrical characterization

Electrical resistance of the uncured/cured LM composites was examined with a two-point probe multimeter (KEW 1018, kyoritsu). For preparing measurements, the uncured samples were screen-printed into a rectangular shape (45 mm in length, 15 mm in width, and 1 mm in height) on glass substrates and the distance between two probes was 1 cm for measuring the resistance. Over limit (O.L.) means that the resistance of the LM composite was more than 40 MΩ.

It is known that a LM composite ($\Phi_{LM} < 0.7$) has electrical insulating properties, because LM is dispersed in the electrical insulating polymer in the form of droplets, and the LM droplets are completely separated

(Jeong et al., 2015). For the concentrated LM composite ($\Phi_{LM} > 0.7$) before and after curing, the results (the resistance > 40 MΩ) showed that the concentrated LM composite was electrically insulating before and after curing. This was because the droplets were still clearly separated by the electrically insulating polymer even at high LM fractions (Figure 1G). Even if droplets contacted each other, the electrically insulating Ga_2O_3 on the LM surface cut off electrical conduction. As h-BN has electrically insulating particles, the LM composite with h-BN also had electrically insulating properties. The internal structure analysis using an X-ray microscope and the size distribution curve of LM droplet size of the diluted sample also show that the LM maintains the droplet shape not only on the surface but also on the inside (Figures S8 and S10).

Numerical details of time dependent heat simulation

IR data preparation for comparative analysis. The IR video is converted into a data matrix in MATLAB (R2020b, Mathworks®) algorithm to find the heat transfer coefficient. We compared the surface temperature with the temperature profile from the numerical simulation, of which details will be explained in the following section. From the grayscale video, the temperature was averaged at the top surface (Figure S12), since the pixel brightness was directly proportional to the surface temperature. The whole area of the top surface was analyzed for a cuboid structure. For the lattice structure, the temperature was averaged in lines, following the center of the top lattice. By the limit of the spatial resolution of the IR camera, the width of a single lattice was narrow, only a few pixels wide. To detect the location of the structures, we used the edge function when the contrast between the structure and background was the maximum (i.e., at the end of heating process, t = 100 [s]).

Heat simulation. The heat transfer through materials was numerically studied using finite element method (FEM) simulation with COMSOL Multiphysics software (v5.6, Comsol Inc.). The time dependent profile of the temperature ($T(t)$) was derived by solving the energy conservation with the Fick's second law as below.

$$(\textit{rate of heat change per volume}) = (\textit{conduction}) + (\textit{convection}) \quad \text{(Equation 4)}$$

$$\rho C_p \frac{dT(t)}{dt} = -\nabla \cdot (k \nabla T(t)) + J \quad \text{(Equation 5)}$$

$$J = h(T_{amb} - T) \quad \text{at the surface} \quad \text{(Equation 6)}$$

$$J = 0 \quad \text{at the bulk} \quad \text{(Equation 7)}$$

where the density (ρ = 4801 kg m^{-3}), specific heat capacity (C_p = 533 J kg^{-1} K^{-1}) and conductivity (k = 9.76 W m^{-1} K^{-1}) followed the composite's properties. Because samples do not flow and have any change in chemical components, mass and momentum conservation are satisfied without calculation. Since only ambient air is heated and flows, its effect on sample temperature is involved by putting T_{amb} and heat transfer coefficient as a function of time. As boundary conditions, the bottom surface is considered as insulated and other surfaces have convection. A graphical scheme for the simulation condition is described in Figure S13.

The simulation geometry is exactly the same as the 3D printing (molding for simple cuboid) model and was divided into computational elements by built-in meshing of COMSOL, where the number of elements was determined by the mesh size dependency test (Figure S14). For the sampling of concentration data, the 3D arc from one diagonal edge point to another was selected. When all the elements totaled 279,601, the result was no different from the simulation with 717,784 elements. Therefore, 279,601 meshes were applied for complex geometry calculations, or same meshing options applied for simple geometry calculations. To achieve adequate calculation accuracy within the limits allowed by computational power (2.1 GHz 24 core CPU, 250 GB RAM), quadratic order discretization was applied for the temperature. Time stepping was set as the intermediate level, while free level time stepping could not apply abrupt changes in the heat transfer coefficient and T_{amb} at the heating-cooling transition.

The convection heat transfer coefficient is determined from T_{sur} of the IR observation at the maximum fitting goodness ($R^2 \geq 0.98$, summarized in Table S1 and displayed in Figure S15), because the air flow is different in heating and cooling processes, h is independently fitted for 4 cases (two structures by two steps). To consider the gradient warming of ambient air ($T_{amb} = T_{amb}(t)$) during the heating process, directly measured air temperature is applied as $T_{amb}(t) = 369.4–69.6 \times 10^{-0.232[1/s]\star t}$ [K]. Generally, the gap between the maximum and minimum temperature of surface was less than a couple of degrees Celsius. Thus, when the color map ranged from 293 to 393 K as in Figure 5A, the entire structure seemed uniform in color and

temperature. Within a narrow color window as Figure S16, however, the spatial gradient of the temperature was recognizable.

Degree of heating (X_h) and cooling (X_c). To normalize the total heat (Q) in each structure, the maximum heat difference was divided by the heat decrement which led to the degree of cooling (X_c). Both Q_{max} and Q_0 were determined only by volume, when T_{amb} was controlled equally (Figure S17).

$$X_c \equiv 1 - X_h = \frac{Q_{max} - Q(t)}{Q_{max} - Q_0} \quad \text{(Equation 8)}$$

When X_h and X_c were plotted against the "cooling" time (t-100[s]), it could be fitted to the exponential decaying function starting from 1 (Figure 5B and inset). Based on the fitted half life time ($=\tau \ln 2$, where τ is the time constant of the decaying function; $e^{-t/\tau}$) each cooling rate was compared for each structure, as summarized in Table S1.